



# Highly efficient solar steam generation of polyamide 6 membrane modified with graphene oxide and Au nanoparticles

Jiaopeng Xu<sup>1</sup>, Yingbo Chen<sup>1,a)</sup> , Ming Cao<sup>1</sup>, Chuanfeng Wang<sup>1</sup>, Pengfei Guo<sup>1</sup>

<sup>1</sup> State Key Laboratory of Separation Membranes and Membrane Processes, School of Materials Science and Engineering, Tiangong University, Tianjin 300387, People's Republic of China

<sup>a)</sup> Address all correspondence to this author. e-mail: bocy2009@hotmail.com; chenyingbo@tiangong.edu.cn

Received: 28 January 2022; accepted: 30 March 2022; published online: 11 April 2022

Solar steam generation (SSG) system greatly improves the efficiency of water evaporation through heat localization, which has broad application prospects at seawater desalination and wastewater treatment. In this paper, polyamide 6-graphene oxide (PA6-GO) membrane was fabricated by nonsolvent-induced phase separation of a solution with GO-modified PA6 in formic acid. Furthermore, the PA6-GO membrane was modified by vacuum filtration of self-assembly gold nanoparticles on its surface for solar stem generation. The composite membrane obtained a light absorption rate of nearly 99.8%. Under the irradiation of  $1 \text{ kW m}^{-2}$ , the evaporation rate of  $1.1 \text{ kg m}^{-2} \text{ h}^{-1}$  was obtained and the evaporation efficiency also reached to 75.6%. The evaporation system has the characteristics of low cost, high stability, strong acid, and alkali corrosion resistance, suggesting great potentials in seawater desalination and sewage treatment.

## Introduction

In recent years, with the continuous development of human society, the ecosystem has been damaged to varying degrees, and the reserves of freshwater resources have also been drastically reduced [1, 2]. People have begun to turn their attention to technologies and energy explorations that can be sustainable and renewable. Among the applications of green energy such as wind energy, nuclear energy, tidal energy, biomass energy, and solar energy [3], the solar energy is considered to be the most valuable for coping with the problems of global water pollution and shortage in the twenty-first century due to its abundant natural reserves and strong renewable capabilities [4]. In the past period of time, people have been working to obtain clean and sanitary drinking water resources from the purification process of sea water and sewage. During this process, scientists have gradually formed the view of thermal plasma [5–7], in which nanoscale hot spots with higher photo-thermal conversion efficiency are generated by absorbing direct solar energy [8, 9]. At the same time, with the rapid development and application of solar technology, such as solar collectors [10, 11], solar thermal power generation [12], photo-thermal therapy [13, 14], small water purification systems [5], large solar concentration systems [15],

solar evaporation [16], it has gradually shown huge practical application value and development potential.

Under the process of solar-driven seawater desalination, the actually evaporation efficiency is determined by the absorption capacity and transfer mode of solar energy. The ideal structure to achieve efficient SSG through the formation of local hot spots usually includes high solar absorption capacity, stable water transport channel, appropriate self-floating capability, and low heat conduction [17, 18]. Among them, high-efficiency broadband light absorption can achieve high photo-thermal transduction efficiency. Low thermal conductivity can effectively reduce thermal loss and improve effective heat utilization ratio. The strong hydrophilicity and porous microstructure can provide well-functioning water conveyance capacity, allowing water vapor to continuously escape from the membrane surface.

Based on the above ideal structure of SSG, a variety of materials and methods have been designed and developed, such as biomass carbon [19, 20], plasma absorbent [21], carbon material [22], and some multi-layer composite materials [23]. According to the principle of bionic bio-interface solar heating, Han, etc. [4] reported stable biomass carbon-based ultra-thin membrane

obtained from eggshell film, whose evaporation rate reached  $1.31 \text{ kg m}^{-2} \text{ h}^{-1}$  under 1 sun ( $1 \text{ kW m}^{-2}$ ) and the actual flow rate obtained was  $1.15 \text{ kg m}^{-2} \text{ h}^{-1}$  in the application of membrane distillation technology. Inspired by transpiration of plant leaves and perspiration of human sweat glands, Wang's team [24] prepared a gold membrane with porous, efficient, and repeatable high-efficiency plasma photo-thermal conversion. The solar steam generation efficiency of 85% was achieved at an illumination power of  $10 \text{ kW m}^{-2}$ . In addition, Li et al. used 3D printing technology [25] to accurately prepare a three-dimensional jellyfish-like solar evaporation system from the composite material of porous carbon black and graphene oxide for the first time. This system has a broadband absorption of 99% in the wavelength range of 250–2500 nm and an energy conversion efficiency of 87.5% at one solar power ( $1 \text{ kW m}^{-2}$ ). Through using the natural channels in the wood structure and the groove morphology on the surface, a series of evaporators coated with carbon nanotubes and graphene oxide (GO) also perform higher evaporation rate and evaporation efficiency [20, 26]. Singamaneni's team reported a double-layer hybrid bio-foam consisting of bacterial nanocellulose and rGO. The foam achieved a solar evaporation efficiency of 83% under  $10 \text{ kW m}^{-2}$  irradiation [27]. In addition, 3D GO foam [16], multifunctional porous GO [28], and green chemically reduced monomer layered GO [6] were also frequently used in exploratory experiments for efficient photo-thermal conversion due to their excellent optical and thermal properties.

In practical applications, carbon-based materials [22, 29] and plasma metals [22] with broadband light absorption properties usually exhibit good thermal conductivity, which contradicts the requirements of local heating and low thermal conductivity [30, 31]. However, this can be overcome by appropriate membrane morphology design and thickness control. It can be said that membrane structure is the decisive factor to determine the overall performance of the system [32, 33]. Therefore, people designed a variety of modes and methods to achieve efficient, stable, and large-scale production of evaporation system.

Therefore, we prepared modified PA6 via in situ polymerization of caprolactam with trace amounts of GO added. Then through the classic nonsolvent-induced phase separation (NIPS) process with inorganic additive lithium chloride (LiCl) as the pore agent, a series of PA6-GO (P-Gx) membranes with bionic "honeycomb" structure for solar evaporation process were carefully constructed. The ratio of pore-forming agent and GO can not only control the pore size distribution, porosity and surface morphology of the membrane [34], but also adjust the formation of heating sites, continuously stable water supply channels on the membrane surface. Finally, the S-AuY/P-Gx composite membranes (S presents the self-assembly; Y represents the pumping volume of Au NPs solution, mL) were obtained by vacuum filtration of the self-assembled Au

nanoparticles (S-Au NPs) [35, 36]. The schematic diagram of whole photo-thermal conversion system is shown in Fig. 1.

## Results and discussion

### Characterization of P-Gx

The surface morphology and cross-sectional structure of the S-Au20/P-G5 and Au20/P-G5 were observed by SEM, as shown in Fig. 2. Figure 2(a) and (e) shows the typical honeycomb morphology of P-G5 with regular pore distribution on the surface. The formation of the honeycomb-like pore structure in the P-Gx would greatly benefit for water evaporation (see Fig. S1) [34, 37]. Figure 2(b) and (f) shows the surface morphology of Au20/P-G5. Au NPs were uniformly dispersed inside and at the edges of the honeycomb, since they were ultrasonically dispersed before preparing the composite membrane. Figure 2(c) is the surface morphology of S-Au20/P-G5. Through the local enlarged image of Fig. 2(g), it can be found that the S-Au NPs aggregated in the pores and made the pore surface rougher. Figure 2(d) is a cross-sectional view of the S-Au20/P-G5 and Fig. 2(h) and (i) shows, respectively, local enlarged views of the lower and upper surfaces. From Fig. 2(h), a skin layer with a thickness of about  $1 \mu\text{m}$  can be observed on the lower surface. From Fig. 2(i), it can be observed that the filter layer of S-Au NPs with a nanoscale thickness was formed after the vacuum filtration process.

In order to further verify the distribution of Au and S-Au NPs on the surface of the P-G5 membranes, we carried out EDS scanning test on Au20/P-G5 and S-Au20/P-G5, as shown in Fig. 3. Au NPs were uniformly distributed [blue in Fig. 3(a)] and the linear assembly S-Au NPs have obvious aggregation [green in Fig. 3(b)]. The distribution and aggregation state of the Au NPs and S-Au NPs was shown in Fig. S2, which was also proved by the color change in Fig. S3. And it was consistent with the reports in literature [38]. In order to verify the leakage of the synthesized Au NPs during the extraction and modification process, UV-Vis was used to test the solution at each stage as shown in Fig. S4.

In order to further detect the valence distribution of Au NPs, XPS was used to detect and analyze the composition of the material surface, including element composition, atomic valence, and energy-level structure. From Fig. 4(a) it is observed that in addition to the absorption peaks of C, N, and O elements in the XPS curve of P-G5, the characteristic peaks of Au NPs also appear in the XPS curves of Au20/P-G5 and S-Au20/P-G5. As shown in Fig. 4(b), two new peaks appeared at 87.6 eV and 84.0 eV, which were attributed to the spectral peaks of Au  $4F_{5/2}$  and Au  $4F_{7/2}$ , respectively, confirming the existence of Au NPs on the membranes [36].

The Raman enhancement effect of P-G5, Au20/P-G5 and S-Au20/P-G5 was tested by Raman spectroscopy, as shown

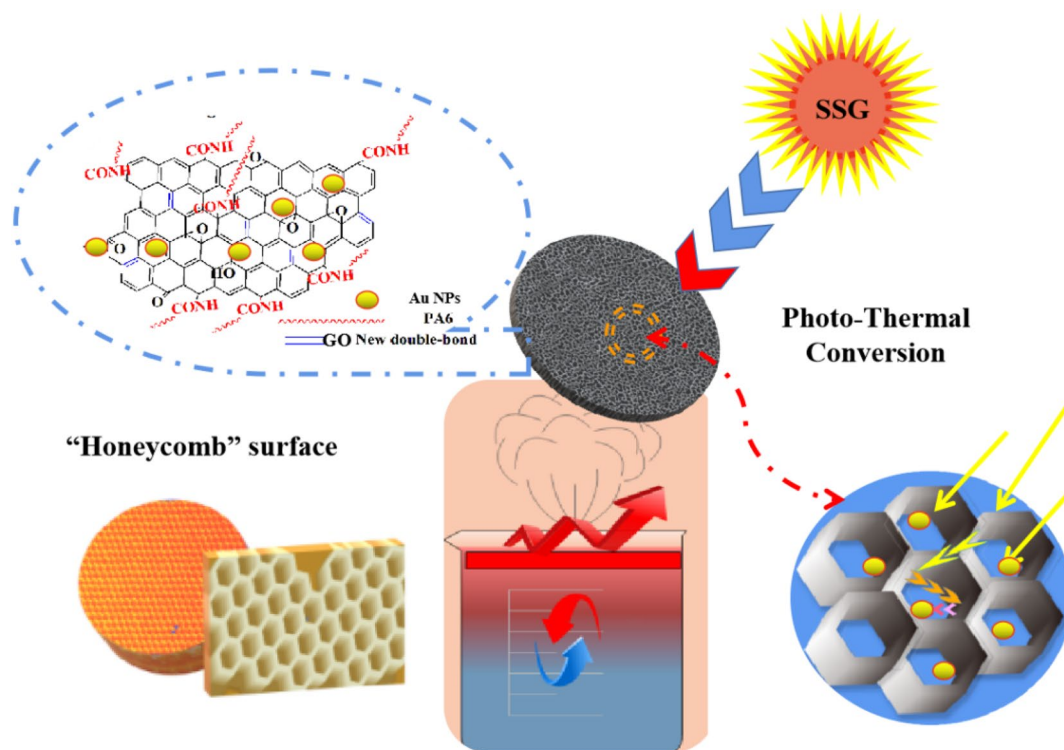


Figure 1: The experimental schematic diagram of the whole photo-thermal conversion system.

in Fig. 5. Two characteristic peaks of P-G5 at  $1327\text{ cm}^{-1}$  and  $1610\text{ cm}^{-1}$ , contributed to the D and G bands of carbon-based materials. Au20/P-G5 and S-Au20/P-G5 have a new peak at  $2134\text{ cm}^{-1}$ , which was mainly related to the addition of Au NPs. The ratio of  $I_D/I_G$  dropped from 1.4 for P-G5 to 1.04 for Au20/P-G5 and 1.25 for S-Au20/P-G5. The decrease in the  $I_D/I_G$  value indicated that the degree of structural defects of the material is reduced, which is mainly caused by the formation of the P-G5 surface filter membrane. And the  $I_D/I_G$  value of Au20/P-G5 was higher than that of S-Au20/P-G5, which was mainly determined by the distribution state of Au NPs on the surface of P-G5.

Meanwhile, as shown in Fig. 6(a) and (b), the transmittance of PA6 membrane (PM) was about 28%; and the reflectance was high to 23%. However, the transmittance ( $T$ ) and reflectance ( $R$ ) of P-G5, Au20/P-G5, and S-Au20/P-G5 were as low as 0.1%. Subsequently, the optical absorption ( $A$ ) of the membrane was over 99.8%, which was calculated according to Eq. (1). This increase was mainly attributed to the introduction of GO carbon-based materials, which reduced the transmittance and reflection of sunlight on the surface of the membrane. And the distribution of surface pores has increased the refraction times of sunlight on the PMs surface and inside, thus greatly improving the absorption efficiency of sunlight and laying a solid foundation for the ultimate goal of high-efficiency solar energy evaporation performance. Metal nanoparticles such as Au NPs have a strong local plasmon resonance effect. The honeycomb surface morphology

of the P-G5 can not only increase the number of refraction of sunlight inside it and further improve the light utilization rate, but also effectively prevent the fall of Au NPs, thereby improving the long-term stability of the entire system.

### The SSG performance

PA6-GO membrane has been successfully applied to solar sea-water desalination due to its high optical absorption characteristics and good stability, as well as its excellent performance of long-term stability, low cost, acid resistance, and alkali corrosion resistance. In order to test the evaporation performance of P-G5 in different acid and alkali environments, the solution in simulated wastewater environment was configured with pH values of 2, 4, 6, 8, and 10, as shown in Fig. S5. The results showed considerable durability and stable evaporation performance. The solar steam generation rate and evaporation efficiency were calculated (Equation S4).

As shown in Fig. 6(c), the water mass loss of S-Au20/P-G5 reached  $0.56\text{ kg m}^{-2}$  and the evaporation rate reached  $1.10\text{ kg m}^{-2}\text{ h}^{-1}$  within 30 min under the optical power of  $1\text{ kW m}^{-2}$  ( $C_{\text{opt}} = 1$ ), which was about 2.72 times of the evaporation rate of ultrapure water (UP) and 2.95 times higher than that of PM. Its evaporation efficiency also reached nearly 75.69%, which was about 2.75 times higher than that of PM. Meanwhile, its temperature difference also reached about  $15^\circ\text{C}$ ,

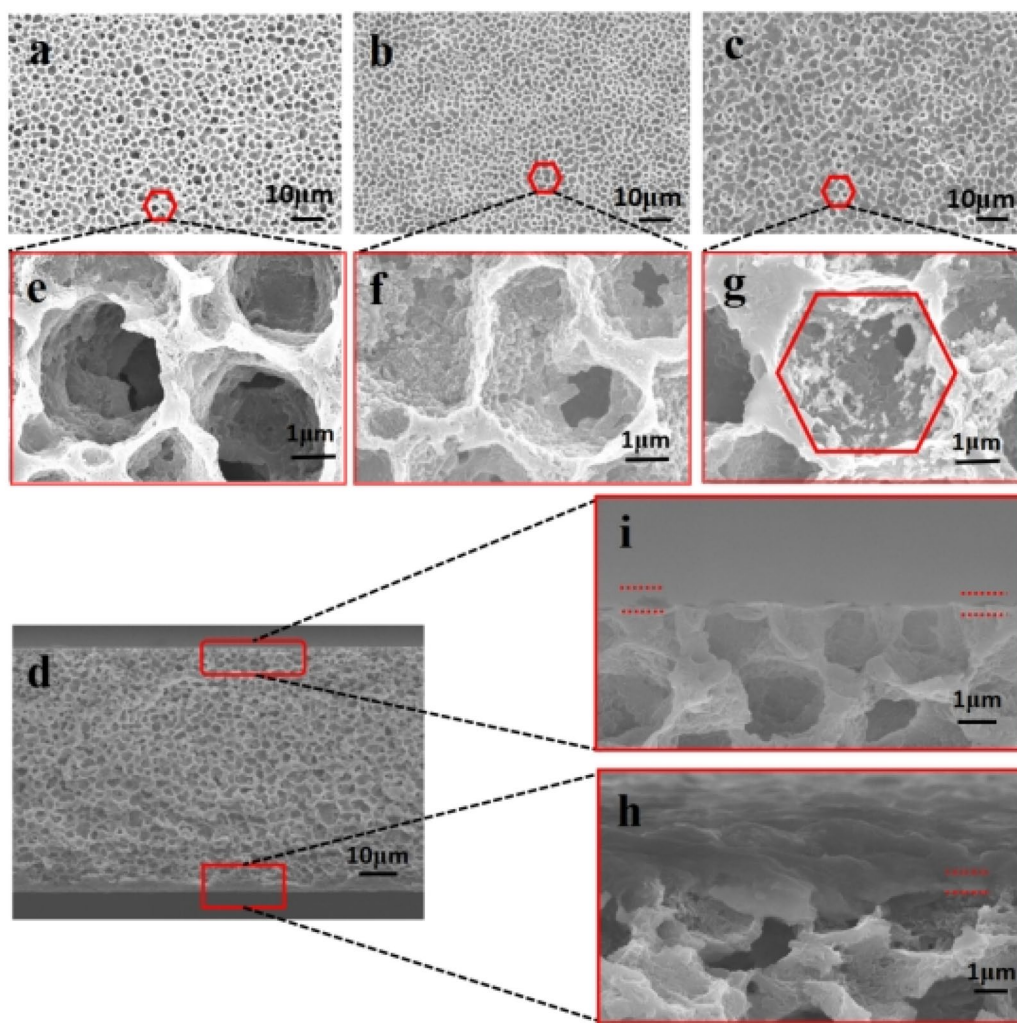


**Figure 2:** The SEM images of composite membrane for surface of P-G5 (a, e); Au20/P-G5 (b, f); S-Au20/P-G5 (c, g); and for cross-section (d, h, i) of S-Au20/P-G5.

as shown in Fig. 6(d). The evaporation efficiency of UP is 27.0%, while the evaporation efficiency of pure PM is only 27.5%, as shown in Fig. 7. This was mainly due to the good thermal conductivity of water body, poor optical absorption performance, and high reflectivity of PM surface. The evaporation efficiency increased from 60.0% of P-G5 to 71.5% of Au20/P-G5 and 75.6% of S-Au20/P-G5. The increase of evaporation efficiency was mainly attributed to the improvement of the porosity and thermal insulation of the material, and the reduction of heat loss. Meanwhile, some studies have shown that the nanometer region between the linearly S-Au NPs could become “Plasmonic Hot Spot.” There were enhancement effects of electromagnetic field and nonconservation of linear momentum in this region, which were more conducive to improving the generation rate of hot electrons [35].

In order to give a more intuitive view of the dynamic heat transfer in the evaporation process, we used FLIR infrared thermal imager to observe and record the front and side temperature distribution of UP and S-Au20/P-G5 before and after 60-min illumination, as shown in Fig. 8. Under  $1 \text{ kW m}^{-2}$ , the surface temperature of pure water is far lower than that of S-Au20/P-G5. Moreover, the difference of the temperature gradient distribution is more obvious. S-Au/PA6-GO has better heat resistance than pure water, therefore, the side temperature on the side presents a gradient distribution from top to bottom. Moreover, most of the heat is mainly used for water evaporation, which reduces heat loss and improves evaporation efficiency.

The comparison of optical absorption rate, evaporation rate, and evaporation efficiency of this work and literature is shown in Table 1. The photo-thermal conversion efficiency of P-G5 was

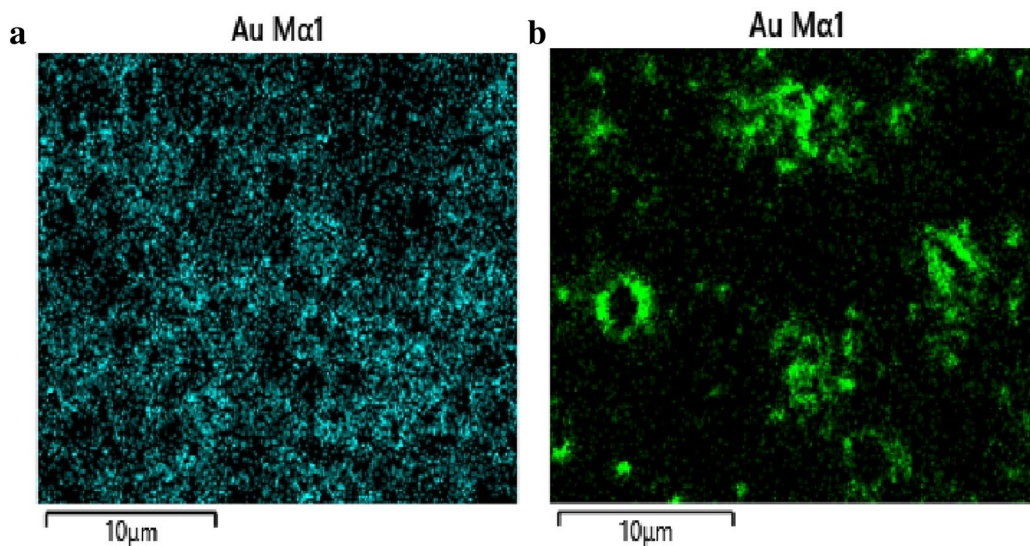


Figure 3: EDS spectra of Au20/P-G5 (a) and S-Au20/P-G5 (b).

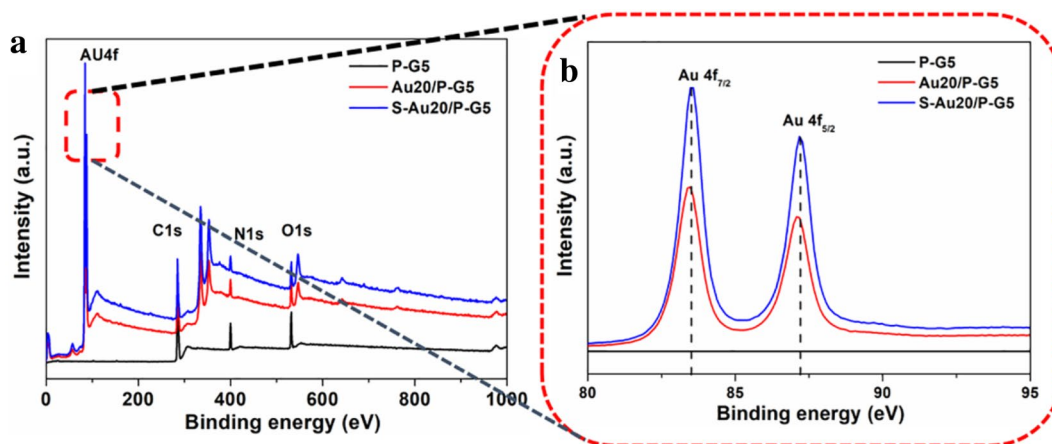


Figure 4: XPS spectra of P-G5, Au20/P-G5 and S-Au20/P-G5 (a) and local magnification at 80–95 eV (b).

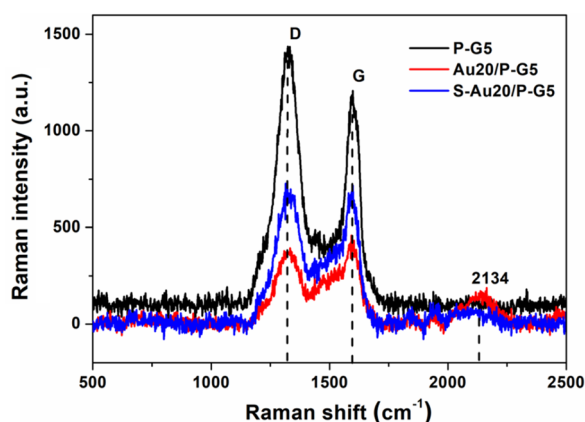


Figure 5: Raman spectra of P-G5, Au20/P-G5 and S-Au20/P-G5.

not greatly improved, but the honeycomb surface morphology made its better optical absorption performance. Moreover, the S-Au20/P-G5 has the characteristics of low cost, high efficiency, and good stability in practical application.

### The application of S-Au20/P-G5 in different conditions

The seawater desalination experiment was simulated. As shown in Fig. 9(a), the conductivity of collected water after evaporation was as low as  $57.19 \mu\text{s cm}^{-1}$ . At the same time, the ICP technology was used to detect the concentrations of four major ions, sodium, magnesium, calcium, and potassium, as shown in Fig. 9(b). The ion concentrations were significantly reduced, which fully met the World Health

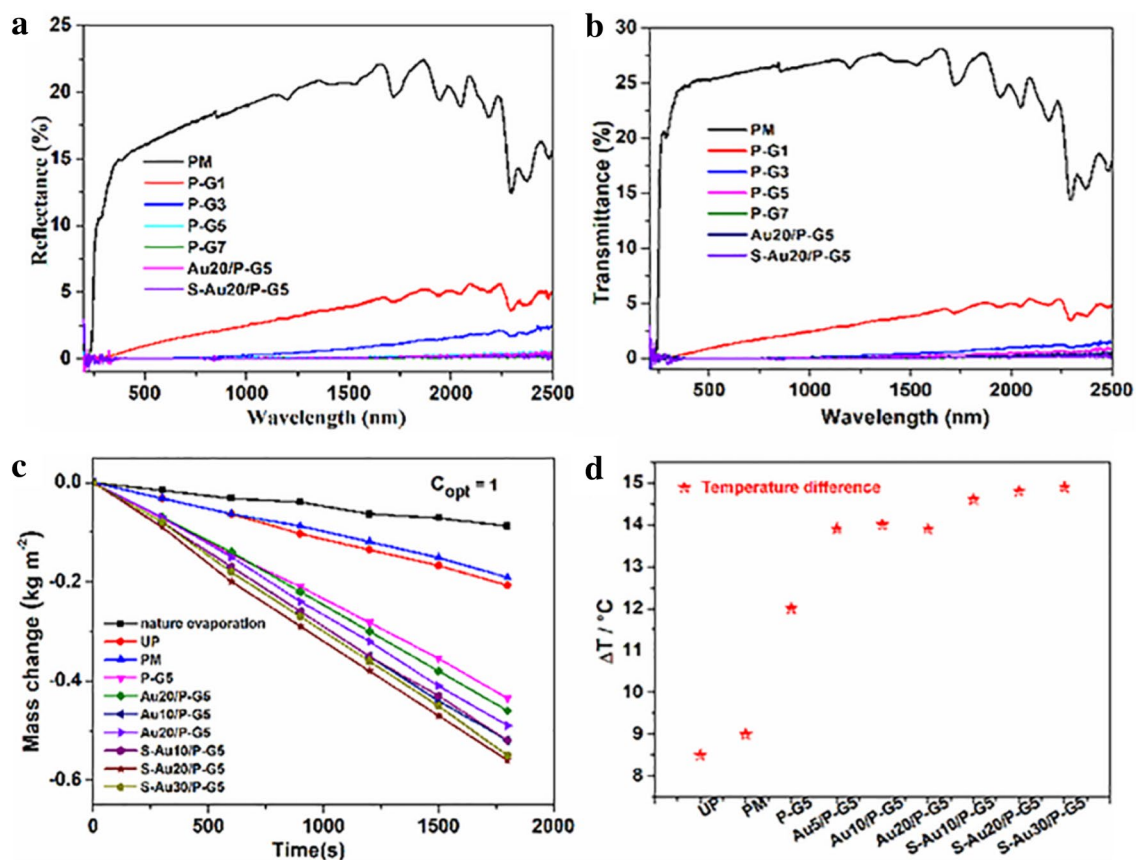


Figure 6: Reflection (a) and transmission (b) spectra of PM, P-Gx, Au20/P-G5, and S-Au20/P-G5; The curved of mass loss of water evaporation (c) and surface temperature difference of membranes (d) under 1 kW m<sup>-2</sup>.

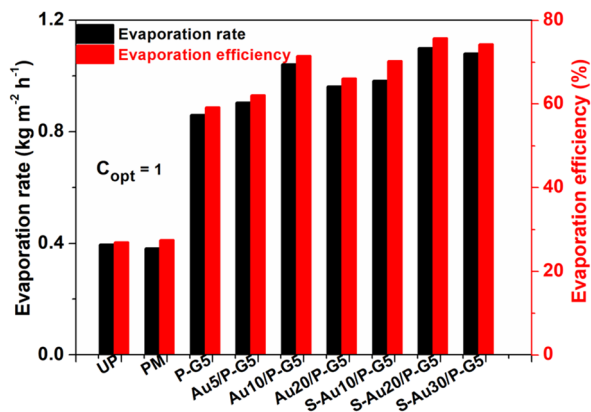


Figure 7: Solar steam generation rate and evaporation efficiency.

Organization standards for healthy drinking water. In order to investigate the performance of S-Au20/P-G5 in wastewater treatment, organic dye solutions of methyl blue (MB) and Congo red (CR) with a concentration of 50 μg mL<sup>-1</sup> were prepared to simulate the dye wastewater environment, as shown in Fig. 9(c) and (d).

The evaporation efficiency of S-AU20 /P-G5 changes with different water quality (Fig. S6). In pure water and simulated seawater, the evaporation efficiency was relatively stable at about 75.6% during the 6-h test period, due to the smooth water contact surface and high photo-thermal conversion of S-Au20 /P-G5. However, when the water quality is changed to an organic dye solution such as methyl blue or Congo red, the evaporation efficiency tended to decrease with time, which may be related to the adsorption of organic dyes on the surface of S-Au20/P-G5. However, the evaporation efficiency can always be more than 70%. The collection device is shown in Fig. 9(e). The practical application performance of S-Au20/P-G5 in dye wastewater treatment was evaluated by measuring the ultraviolet absorbance of the raw wastewater solution and the collected water. The characteristic absorption peak of the dye can be observed in the figure, while the absorbance of the collected water is nearly zero, indicating that S-Au20/P-G5 has a high purification capacity in sewage treatment. Changes in evaporation rate of S-Au20/PA6-GO in multiple cycles within 48 h are shown in Fig. 9(f). In the long-term use process, S-Au20/P-G5 can maintain good stability while ensuring a high evaporation rate. Meanwhile, it showed that the crystallization adsorption of salt was

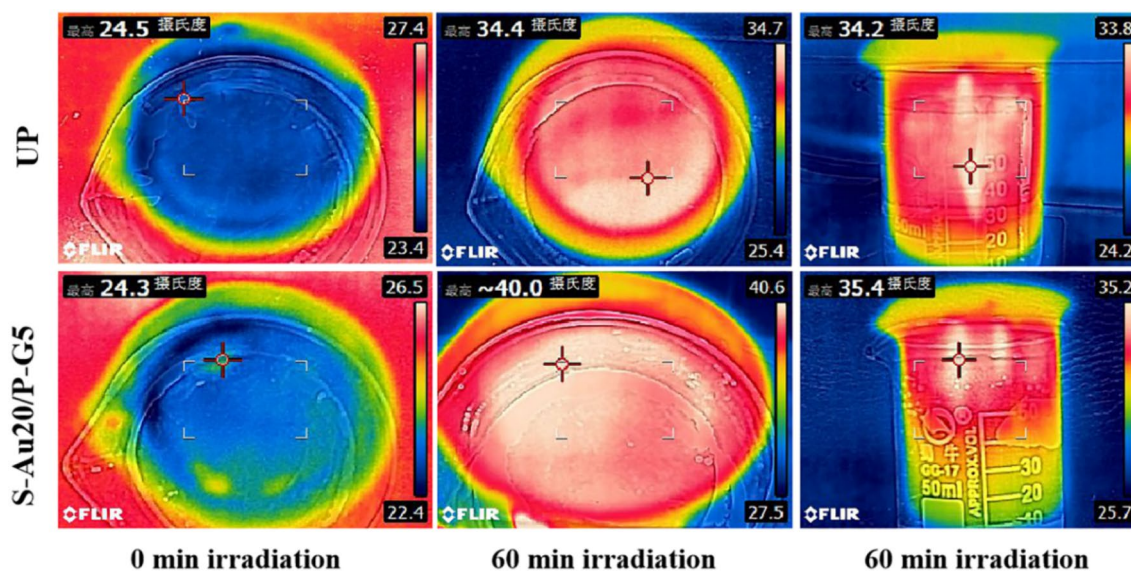


Figure 8: The infrared thermal image of temperature distribution on the surface and side of UP and S-Au20/P-G5 before and after illumination.

TABLE 1: Performance comparison.

Materials	Optical absorption efficiency (%)	Evaporation rate ( $\text{kg m}^{-2} \text{h}^{-1}$ )	Evaporation efficiency (%)	Irradiation power ( $\text{kW m}^{-2}$ )	Refs.
Biomass carbon materials	95	1.08	68.0	1	[19]
Black phosphorous nanosheets	~	0.94	64.6	1	[39]
CB/GO	99	0.89	61.2	1	[40]
rGO/mixed cellulose	~	0.84	60.0	1	[6]
Flame-Treated Wood	99	~0.90	72.0	1	[41]
Carbonized rice husk foam	92	1.03	71.0	1	[42]
Au NPs/PMs	90	~	85.0	10	[24]
Blanck Au	89	1.92	65.2	1	[22]
Black Ni	89	1.92	65.4	1	[22]
Biomass carbonized particles	98	0.96	70.0	1	[43]
Magnetic $\text{MoS}_2$	96	~	79.2	2.5	[44]
P-G5	99.8	0.86	60.0	1	This work
S-Au20/P-G5	99.8	1.16	75.6	1	

not enough to affect the evaporation performance of S-Au20/P-G5 during the experiment. It was mainly due to the grafting of GO that the water contact surface tends to be smooth and the formation of salt scaling on the surface of the membrane is weakened. At the same time, due to the strong water absorption of the material itself, the water supply capacity is also guaranteed.

## Conclusion

In summary, S-Au20/P-G5 was fabricated by vacuum filtration of self-assembly Au NPs on the PA6-GO5 substrate. At the wavelength range of 200–2500 nm, the absorption rate was nearly 99.8%. Under the optical power density of  $1 \text{ kW m}^{-2}$ , the evaporation rate increased to  $1.1 \text{ kg m}^{-2} \text{ h}^{-1}$  and the evaporation

efficiency also reached 75.6%. At the same time, S-Au20/P-G5 has also shown excellent practical value and potential in the application of seawater desalination and sewage treatment.

## Methods

### Chemicals

Powder GO (single layer, 300 mesh) was purchased from Suzhou Hengqiu Technology Co., Ltd. Caprolactam (99%), 6-aminocaproic acid (99%), tetrachloroauric acid trihydrate Chemicals, sodium citrate (analytical purity), Congo Red (CR), and Methyl Blue (MB) were purchased from Shanghai Aladdin Biochemical Technology Co., Ltd. Sodium chloride

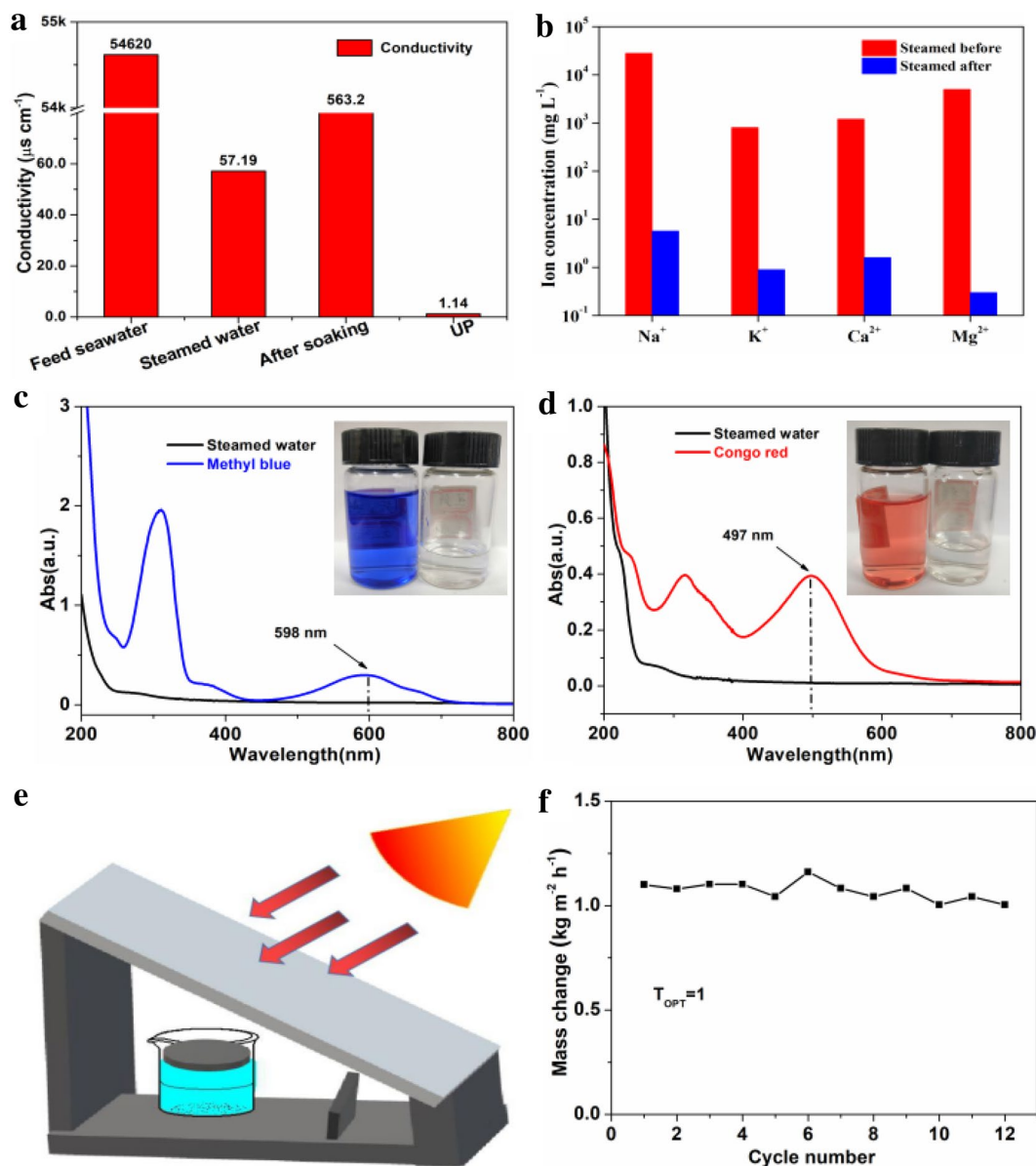


**Figure 9:** The conductivity test of collected water (a) and ion content changes of simulated seawater (b); UV absorbance curve before and after dye wastewater treatment, MB (c), CR (d); diagram of recovery device for solar evaporation experiment (e); long-term stability test curve (f).

( $\geq 99.5\%$ ) and ammonia (analytical purity) were obtained from Tianjin Fengchuan Chemical Reagent Technology Co., Ltd. Anhydrous magnesium sulfate ( $\geq 99.0\%$ ) and formic acid (AR  $\geq 88.0\%$ ) were obtained from Tianjin Kemeou Kermel Chemical Reagent Co., Ltd. Calcium chloride was purchased from Shanghai Titan Technology Co., Ltd. Potassium chloride (99.5%) was purchased from Tianjin Guangfu Technology Development Co., Ltd. Ultrapure water (UP,  $18.25 \text{ M}\Omega \text{ cm}^{-1}$ ) was made by the laboratory. All chemicals were used as received without further purification.

### Characterizations

Phenom XL desktop scanning electron microscope (SEM) was used to observe the surface morphology of the sample at 5 kV. X-ray photoelectron spectrometer (K-alpha type, XPS) was used to detect the surface composition of S-AuY/P-Gx and AuY/P-Gx. The laser confocal Raman spectroscopy (XploRA PLUS) was used to characterize the structure of the sample in the wave-number range of  $400\text{--}2500 \text{ cm}^{-1}$ . The Ultraviolet-Visible-Near Infrared spectrometer (UH4150) equipped with a 60 mm stand-ard integrating sphere was used to measure the light reflection



(*R*) and transmission (*T*) spectra of the sample in the range of 200–2500 nm. Subsequently, the optical absorption (*A*) of the membrane was calculated according to Eq. (1) [24]:

$$A (\%) = 1 - R - T \quad (1)$$

The AR2202CN electronic balance with an accuracy of 0.1 g was used to record the water quality changes in real time. The evaporation experiment was carried out using a solar simulator (CEL-S500/350 xenon light source), which was equipped with a standard AM1.5G optical filter. The distribution of Au NPs on the surface of P-G5 was observed and determined using an energy spectrometer mounted on a thermal field electron microscope. A transmission electron microscope with the instrument model Hitachi H7650 was used to observe and analyze the particle size and morphology of the Au NPs. Before the testing, the samples were sprayed with platinum.

### Preparation of PA6-GOx (P-Gx) membranes

A casting solution containing 20 wt% P-Gx (more details on the fabrication of P-Gx are shown in section S1 and Fig. S7) was prepared by dissolving it in formic acid at room temperature with magnetic stirring for 12 h, and  $x = 1, 3, 5, 7$  represent the mass ratios of graphene oxide = 0.1, 0.3, 0.5, 0.7 wt%, respectively [37]. Pore-forming agent (5 wt% LiCl) was added to adjust the porosity and pore size distribution of the membranes. Then, the casting solution was put in an oven (– 0.6 MPa) for vacuum defoaming for 60 min. A membrane with a thickness of 200  $\mu\text{m}$  was scraped on a glass plate at a constant speed (Fig. S8). After stabilizing for 10 s, the glass plate was immersed in a solidification bath of pure water. The prepared PA6 membrane and the membranes containing with GO were called as PM and P-Gx ( $x$  indicated the weight percentage of GO in the PA6-GO), respectively.

### Modification process of Au NPs

A traditional sodium citrate method was used to synthesize Au NPs (more details are shown in section S2). 15 mL Au NPs in a 50 mL centrifuge tube was centrifuged at 12,000 rpm for 15 min. After removing the supernatant, the residuum was dispersed in 18 mL ethanol and treated in ultrasonic device under 400 W for 10 min to make the dispersion uniform. Chain self-assembly process was carried out by dropwise adding 400–2000  $\mu\text{L}$  5.0 mM NaCl solution and 10–20  $\mu\text{L}$  water after stabilization. Subsequently standing for 30 min, 10 mL 4.2 vol% ethanol ammonia solution was quickly added to promote the self-assembly process. Finally, the color of the solution changed from purple-red to blue (Fig. S3), indicating the occurrence of self-assembly process (S-Au) [35, 36].

### Preparation of AuY/P-Gx and S-AuY/P-Gx membranes

AuY/P-Gx and S-AuY/P-Gx membranes were prepared by vacuum filtration under – 0.1 MPa, as shown in Fig. S9. Y indicated the filtration volume (10 mL, 20 mL, 30 mL) of Au NP and S-Au NPs on the P-Gx supporting layer.

### Solar evaporation performance test

The prepared membranes were cut into pieces of the required size (1.8 cm  $\times$  1.8 cm). The membranes were naturally suspended on the ultrapure water (UP) in a beaker for SSG. The test was conducted at about 25  $^{\circ}\text{C}$  and the relative humidity about 35–45%. The light intensity was measured with a strong light power meter, surrounded by polystyrene foam as an insulation material. After stabilized for 30 min under illumination, evaporation quality was recorded in real time by setting the beaker on an electronic balance (calculation method was shown in the section S3). At the same time, the temperature change on membrane surface was recorded with an infrared thermography.

With reference to the above experimental process, the acid–base tolerance test of the membranes was carried out in aqueous solutions with pH 2, 4, 6, 8, and 10. And 50 mg/mL methyl blue (MB) and methyl orange (MO) organic dye solutions were prepared to simulate wastewater solution. Seawater solution containing a variety of salts was simulated to test the performance of the membranes in practical applications. The purification effect of organic dyes was detected by UV-1100 ultraviolet spectrophotometer and the pH of the solution was measured by a pH meter.

### Acknowledgments

This work was financially supported by Key R&D program of Tianjin municipal science and technology commission (20YFZCSN00930).

### Data availability

All data generated or analyzed during this study are included in this published article.

### Declarations

**Conflict of interest** The authors declare that they have no known competing financial interests or personal relationships that could have appeared to influence the work reported in this paper.

### Supplementary Information

The online version contains supplementary material available at <https://doi.org/10.1557/s43578-022-00552-y>.

## References

1. L. Zhao, Q. Yang, W. Guo, H. Liu, T. Ma, F. Qu, Co<sub>2</sub>67S<sub>4</sub>-based photothermal membrane with high mechanical properties for efficient solar water evaporation and photothermal antibacterial applications. *ACS Appl. Mater. Interfaces* **11**, 20820–20827 (2019)
2. C. Chen, Y. Li, J. Song, Z. Yang, Y. Kuang, E. Hitz, C. Jia, A. Gong, F. Jiang, J.Y. Zhu, B. Yang, J. Xie, L. Hu, Highly flexible and efficient solar steam generation device. *Adv. Mater.* **29**, 1701756 (2017)
3. Y. Liu, Y. Zhang, G. Jia, Photothermal conversion of Bi<sub>2</sub>Se<sub>3</sub> nanosheets and efficient steam generation by capillary siphoning. *Energy Rep.* **6**, 1304–1311 (2020)
4. X. Han, W. Wang, K. Zuo, L. Chen, L. Yuan, J. Liang, Q. Li, P.M. Ajayan, Y. Zhao, J. Lou, Bio-derived ultrathin membrane for solar driven water purification. *Nano Energy* **60**, 567–575 (2019)
5. M.A. Shannon, P.W. Bohn, M. Elimelech, J.G. Georgiadis, B.J. Marinas, A.M. Mayes, Science and technology for water purification in the coming decades, in *Nanoscience and Technology*, (2009) pp. 337–346.
6. G. Wang, Y. Fu, X. Ma, W. Pi, D. Liu, X. Wang, Reusable reduced graphene oxide based double-layer system modified by polyethylenimine for solar steam generation. *Carbon* **114**, 117–124 (2017)
7. G. Baffou, R. Quidant, F.J.G. de Abajo, Nanoscale control of optical heating in complex plasmonic systems. *ACS Nano* **4**, 709–716 (2010)
8. Z.Y. Fang, Y.R. Zhen, O. Neumann, A. Polman, F.J.G. de Abajo, P. Nordlander, N.J. Halas, Evolution of light-induced vapor generation at a liquid-immersed metallic nanoparticle. *Nano Lett.* **13**, 1736–1742 (2013)
9. N.J. Halas, O. Neumann, A. Urban, N. Hogan, Z.Y. Fang, A. Pimpinelli, S. Lal, P. Nordlander, Solar vapor generation enabled by nanoparticles. *Abstr. Pap. Am. Chem. Soc.* **246**, 42–49 (2013)
10. J.L. Li, D. Day, M. Gu, Ultra-low energy threshold for cancer photothermal therapy using transferrin-conjugated gold nanorods. *Adv. Mater.* **20**, 3866–3871 (2008)
11. H.Y. Liu, D. Chen, L.L. Li, T.L. Liu, L.F. Tan, X.L. Wu, F.Q. Tang, Multifunctional gold nanoshells on silica nanorattles: a platform for the combination of photothermal therapy and chemotherapy with low systemic toxicity. *Angew. Chem.-Int. Ed.* **50**, 891–895 (2011)
12. M. Reisman, J.C. Bretschneider, G. von Plessen, U. Simon, Reversible photothermal melting of DNA in DNA-gold-nanoparticle networks. *Small* **4**, 607–610 (2008)
13. K. Manthiram, A.P. Alivisatos, Tunable localized surface plasmon resonances in tungsten oxide nanocrystals. *J. Am. Chem. Soc.* **134**, 3995–3998 (2012)
14. J.C. Liu, O. Margeat, W. Dachraoui, X.J. Liu, M. Fahlman, J. Ackermann, Gram-scale synthesis of ultrathin tungsten oxide nanowires and their aspect ratio-dependent photocatalytic activity. *Adv. Funct. Mater.* **24**, 6029–6037 (2014)
15. M.K. Gupta, S.C. Kaushik, Exergy analysis and investigation for various feed water heaters of direct steam generation solar-thermal power plant. *Renew. Energy* **35**, 1228–1235 (2010)
16. W. Fang, L. Zhao, H. Chen, X. He, W. Li, X. Du, Z. Sun, T. Zhang, Y. Shen, Graphene oxide foam fabricated with surfactant foaming method for efficient solar vapor generation. *J. Mater. Sci.* **54**, 12782–12793 (2019)
17. X. Zhao, X.-J. Zha, J.-H. Pu, L. Bai, R.-Y. Bao, Z.-Y. Liu, M.-B. Yang, W. Yang, Macroporous three-dimensional MXene architectures for highly efficient solar steam generation. *J. Mater. Chem. A* **7**, 10446–10455 (2019)
18. F. Zhao, Y.H. Guo, X.Y. Zhou, W. Shi, G.H. Yu, Materials for solar-powered water evaporation. *Nat. Rev. Mater.* **5**, 388–401 (2020)
19. M. Zhu, A. Xia, Q. Feng, X. Wu, C. Zhang, D. Wu, H. Zhu, Biomass carbon materials for efficient solar steam generation prepared from carbonized enteromorpha prolifera. *Energy Technol.* **8**, 1901215 (2019)
20. F. Jiang, T. Li, Y. Li, Y. Zhang, A. Gong, J. Dai, E. Hitz, W. Luo, L. Hu, Wood-based nanotechnologies toward sustainability. *Adv. Mater.* **30**, 1703453 (2018)
21. G. Li, F. Li, J. Liu, C.J.J.S.S.C. Fan, Fe-based MOFs for photocatalytic N<sub>2</sub> reduction: key role of transition metal iron in nitrogen activation. *J. Solid State Chem.* **285**, 121245 (2020)
22. Y. Chen, C. Sha, W. Wang, F. Yang, Solar-driven steam generation on nitrogen-doped graphene in a 2D water path isolation system. *Mater. Res. Express* **7**, 015507 (2020)
23. S.H. Hong, Y. Shi, R.Y. Li, C.L. Zhang, Y. Jin, P. Wang, Nature-inspired, 3D origami solar steam generator toward near full utilization of solar energy. *ACS Appl. Mater. Interfaces* **10**, 28517–28524 (2018)
24. X. Wang, Y. He, X. Liu, G. Cheng, J. Zhu, Solar steam generation through bio-inspired interface heating of broadband-absorbing plasmonic membranes. *Appl. Energy* **195**, 414–425 (2017)
25. Y. Li, T. Gao, Z. Yang, C. Chen, W. Luo, J. Song, E. Hitz, C. Jia, Y. Zhou, B. Liu, B. Yang, L. Hu, 3D-printed, all-in-one evaporator for high-efficiency solar steam generation under 1 sun illumination. *Adv. Mater.* **29**, 1700981 (2017)
26. K.K. Liu, Q. Jiang, S. Tadepalli, R. Raliya, P. Biswas, R.R. Naik, S. Singamaneni, Wood-graphene oxide composite for highly efficient solar steam generation and desalination. *ACS Appl. Mater. Interfaces* **9**, 7675–7681 (2017)
27. Q.S. Jiang, L.M. Tian, K.K. Liu, S. Tadepalli, R. Raliya, P. Biswas, R.R. Naik, S. Singamaneni, Bilayered biofoam for highly efficient solar steam generation. *Adv. Mater.* **28**, 9400–9407 (2016)
28. Y. Ito, Y. Tanabe, J. Han, T. Fujita, K. Tanigaki, M. Chen, Multifunctional porous graphene for high-efficiency steam generation by heat localization. *Adv. Mater.* **27**, 4302–4307 (2015)

29. H.T. Kieu, K. Zhou, A.W.K. Law, Surface morphology effect on the evaporation of water on graphene oxide: a molecular dynamics study. *Appl. Surf. Sci.* **488**, 335–342 (2019)
30. Y. Chang, Z. Wang, Y.-E. Shi, X. Ma, L. Ma, Y. Zhang, J. Zhan, Hydrophobic W18O49 mesocrystal on hydrophilic PTFE membrane as an efficient solar steam generation device under one sun. *J. Mater. Chem. A* **6**, 10939–10946 (2018)
31. G. Ni, G. Li, S.V. Boriskina, H.X. Li, W.L. Yang, T.J. Zhang, G. Chen, Steam generation under one sun enabled by a floating structure with thermal concentration. *Nat. Energy* **1**, 16126 (2016)
32. A. Politano, P. Argurio, G. Di Profio, V. Sanna, A. Cupolillo, S. Chakraborty, H.A. Arafat, E. Curcio, Photothermal membrane distillation for seawater desalination. *Adv. Mater.* **29**, 1603504 (2017)
33. Y. Xu, D. Liu, H. Xiang, S. Ren, Z. Zhu, D. Liu, H. Xu, F. Cui, W. Wang, Easily scaled-up photo-thermal membrane with structure-dependent auto-cleaning feature for high-efficient solar desalination. *J. Membr. Sci.* **586**, 222–230 (2019)
34. J. Hou, C. Bao, S. Qu, X. Hu, S. Nair, Y. Chen, Graphene oxide membranes for ion separation: detailed studies on the effects of fabricating conditions. *Appl. Surf. Sci.* **459**, 185–193 (2018)
35. Z. Yin, Y. Wang, C. Song, L. Zheng, N. Ma, X. Liu, S. Li, L. Lin, M. Li, Y. Xu, W. Li, G. Hu, Z. Fang, D. Ma, Hybrid Au-Ag nanostructures for enhanced plasmon-driven catalytic selective hydrogenation through visible light irradiation and surface-enhanced Raman scattering. *J. Am. Chem. Soc.* **140**, 864–867 (2018)
36. X. Han, J. Goebel, Z. Lu, Y. Yin, Role of salt in the spontaneous assembly of charged gold nanoparticles in ethanol. *Langmuir* **27**, 5282–5289 (2011)
37. Z. Xu, C. Gao, In situ polymerization approach to graphene-reinforced nylon-6 composites. *Macromolecules* **43**, 6716–6723 (2010)
38. Z. Yin, W. Zhang, Q. Fu, H. Yue, W. Wei, P. Tang, W. Li, W. Li, L. Lin, G. Ma, D. Ma, Construction of stable chainlike Au nanostructures via silica coating and exploration for potential photothermal therapy. *Small* **10**, 3619–3624 (2014)
39. Z. Li, W. Cai, X. Wang, Y. Hu, Z. Gui, Self-floating black phosphorous nanosheets as a carry-on solar vapor generator. *J. Colloid Interface Sci.* **582**, 496–505 (2020)
40. Y. Li, T. Gao, Z. Yang, C. Chen, Y. Kuang, J. Song, C. Jia, E.M. Hitz, B. Yang, L. Hu, Graphene oxide-based evaporator with one-dimensional water transport enabling high-efficiency solar desalination. *Nano Energy* **41**, 201–209 (2017)
41. G. Xue, K. Liu, Q. Chen, P. Yang, J. Li, T. Ding, J. Duan, B. Qi, J. Zhou, Robust and low-cost flame-treated wood for high-performance solar steam generation. *ACS Appl. Mater. Interfaces* **9**, 15052–15057 (2017)
42. W. Fang, L. Zhao, X. He, H. Chen, W. Li, X. Zeng, X. Chen, Y. Shen, W. Zhang, Carbonized rice husk foam constructed by surfactant foaming method for solar steam generation. *Renew. Energy* **151**, 1067–1075 (2020)
43. C. Boo, Y. Wang, I. Zucker, Y. Choo, C.O. Osuji, M. Elimelch, High performance nanofiltration membrane for effective removal of perfluoroalkyl substances at high water recovery. *Environ. Sci. Technol.* **52**, 7279–7288 (2018)
44. Q. Wang, Y. Qin, F. Jia, Y. Li, S. Song, Magnetic MoS<sub>2</sub> nanosheets as recyclable solar-absorbers for high-performance solar steam generation. *Renew. Energy* **163**, 146–153 (2021)